ELSEVIER

Journal of Alloys and Compounds 434–435 (2007) 126–130

Journal of ALLOYS AND COMPOUNDS

www.elsevier.com/locate/jallcom

Phase separation and nanocrystal formation in Al-based metallic glasses

Jerzy Antonowicz

Faculty of Physics, Warsaw University of Technology, Koszykowa 75, 00-662 Warsaw, Poland

Available online 9 October 2006

Abstract

Nanocrystallization in a group of Al–RE and Al–RE–TM (RE = rare earth, TM = transition metal) melt-spun amorphous alloys was studied using in situ small- and wide-angle X-ray scattering techniques (SAXS/WAXS) and transmission electron microscopy (TEM). The SAXS/WAXS measurements were carried out during isothermal annealing at temperatures close to crystallization point. A continuously growing interference maximum shifting progressively toward lower angles was found to develop in SAXS regime. Simultaneously taken WAXS spectra reveal formation of the primary fcc-Al nanocrystalline phase. The presence of the SAXS signal maximum indicates the spatial correlation between the compositional fluctuations. The peak position decay is an evidence of an increase of the fluctuation spacing characteristic for the coarsening stage of phase separation. The SAXS/WAXS data analysis indicates that amorphous phase decomposition triggers and controls the fcc-Al nanocrystalline phase formation. The glassy phase initially decomposes into Al-rich and RE-rich regions with typical lengths scale of about 10 nm. The nanocrystals nucleate preferentially inside the Al-rich amorphous regions and their growth is constrained by the region size because of the sluggish atomic diffusion in the RE-rich zones. A different crystallization mechanism is demonstrated in Al–Y–Ni–Co glass where WAXS spectra show formation of the fcc-Al primary phase but no interference peak in SAXS regime was found.

Keywords: Amorphous materials; Nanostructures; Precipitation; Synchrotron radiation

1. Introduction

Aluminium-based amorphous alloys are known to exhibit unique mechanical properties [1]. Thermal annealing of these glasses often leads to formation of the nanocrystalline microstructure. This kind of structure consists of ∼10 nm fcc-Al grains of a density of $\sim 10^{23}$ m^{-3} embedded in an amorphous matrix. The partial crystallization of the glass leads to further improvement of its' mechanical properties and allows obtaining material with superior strength-to-weight ratio [2]. The nanocrystallization process requires ultra-high nucleation frequency and sluggish grain growth. Formation of nanocrystals in the Al-based glasses was previously attributed to heterogeneous nucleation [3], "quenched-in" nuclei [4] and new type of homogeneous nucleation [5]. Recently the phase separation at length scale of ∼40 nm in Al–Gd–La–Ni glass was reported with nanocrystals nucleating preferentially on the boundaries between the two phases [6,7]. The rapid crystal growth arrest was explained by overlapping of the diffusion fields of adjacent crystals [8].

Our recent results on crystallization kinetics in Al–RE glasses [9,10] indicate that crystal growth exhibits sharp transition between initially rapid and very sluggish kinetics in later stages of a single grain evolution. Similar nanocrystal growth kinetics in Al-based glasses was also suggested in earlier works [3,11]. We concluded that the nanocrystallization process is controlled by nucleation rate. The amorphous phase separation was proposed as one of the possible origins of the observed crystallization kinetics. Experimental evidences of phase separation in numerous metallic glasses basing on the small-angle X-ray and neutron scattering [12–14], X-ray diffraction [14], differential scanning calorimetry [15], transmission electron microscopy [16,6,7] and atom probe field ion microscopy [17,18] were reported over previous years. The relation between the amorphous phase separation and the subsequent crystallization behavior was discussed [13,14,19,20]. Both experimental results and theoretical considerations indicate that phase separation occurrence prior to crystallization leads to refinement of the resulting microstructure.

The present paper reports results obtained for a group of Al–RE and Al–RE–TM amorphous alloys during in situ, time resolved, combined small- and wide-angle X-ray scattering (SAXS/WAXS) supported by transmission electron microscopy (TEM) analysis.

E-mail address: antonowi@if.pw.edu.pl.

0925-8388/$ – see front matter © 2006 Published by Elsevier B.V.
doi:10.1016/j.jallcom.2006.08.152

2. Experimental

The ingots of investigated alloys were prepared from pure elements using arc-melting device. The nominal compositions of thus prepared alloys were: $Al_{90}Y_{10}$, $Al_{92}Sm_8$, $Al_{91}Gd_9$, $Al_{91}Tb_9$, $Al_{90}Sm_8Ni_2$, $Al_{84}Y_9Ni_5Co_2$. Amorphous samples in form of 20–30 μm thick ribbons were produced by rapid quenching using melt-spinning device with wheel speed of 33–40 m/s.

The SAXS/WAXS experiment was performed at ID02 beamline of the European Synchrotron Radiation Facility (ESRF). The spectra were collected in transmission mode with the sample placed between the incident beam and the SAXS/WAXS detectors. The incident beam wavelength λ used was 1.00 Å corresponding to energy of 12.5 keV. The SAXS sample-detector distance was 3 m allowing the q range of 0.07–2.1 nm^{-1}, where $q = (4\pi/\lambda)\sin\theta$ and θ is half the scattering angle. The WAXS measurements covered 5–54° of 2θ range. Pieces of as-quenched ribbons were sealed in Pyrex capillaries under argon atmosphere and placed in DSC-type *Linkam* hot-stage fixed between the incident beam and the detectors. The SAXS/WAXS spectra were taken simultaneously every 15–20 s with acquisition time of 0.5 s. The 2D scattered intensity patterns were azimuthally averaged to obtain 1D scattering curves $I(q)$. All investigated alloys exhibited fully amorphous diffraction pattern in as-quenched state. The annealing temperature was reached with 90 K/min heating rate and the temperature was stabilized with precision of 1°. The TEM specimen was prepared by ion-milling and analyzed using Jeol 3010 microscope.

3. Results and discussion

It was found that $Al_{90}Y_{10}$, $Al_{92}Sm_8$, $Al_{91}Gd_9$, $Al_{91}Tb_9$ and $Al_{90}Sm_8Ni_2$ samples exhibit similar SAXS/WAXS spectra evolution. Fig. 1 presents the SAXS/WAXS spectra of investigated amorphous alloys treated in different annealing conditions. The detailed analysis of the SAXS/WAXS data supported by TEM

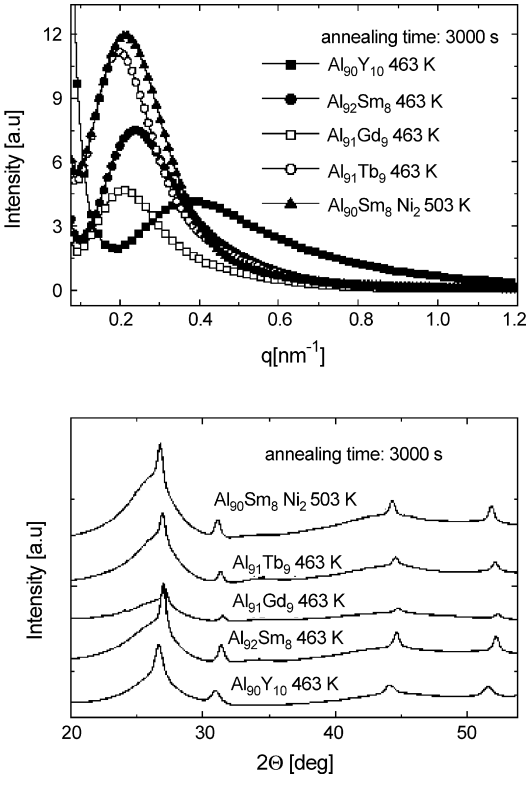

Fig. 1. SAXS (top) and WAXS (bottom) spectra of $Al_{90}Y_{10}$, $Al_{92}Sm_8$, $Al_{91}Gd_9$, $Al_{91}Tb_9$ and $Al_{90}Sm_8Ni_2$ amorphous alloys treated in different annealing conditions.

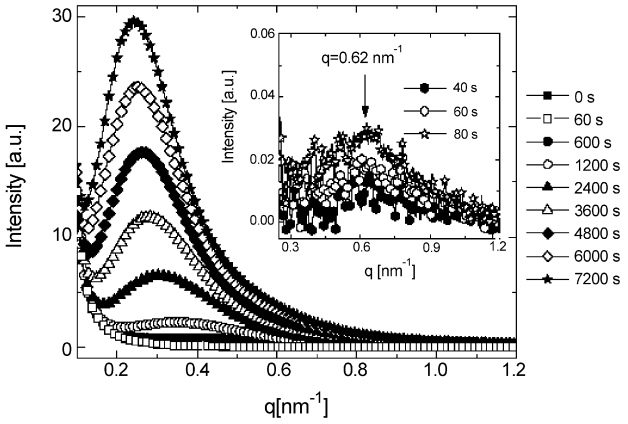

Fig. 2. Small-angle spectra evolution during isothermal annealing at 443 K of an as-quenched $Al_{92}Sm_8$. The inset presents early stages of SAXS maximum development when the peak is centered at $q = 0.62\ nm^{-1}$.

results for $Al_{92}Sm_8$ amorphous alloy are given in following part of this paragraph.

Fig. 2 presents the time evolution of SAXS spectra of $Al_{92}Sm_8$ amorphous alloy during annealing at 443 K. The annealing temperature was chosen 5° above the crystallization onset point determined from the DSC thermogram at 10 K/min. The SAXS intensity $I(q)$ exhibits an interference maximum decaying to extrapolated value of $I(0) = 0$. The peak develops growing continuously with time and shifting toward lower q values. The presence of a significant constant signal contribution at low q is attributed to scattering from the sample surface imperfections. The early stage of the SAXS peak evolution is demonstrated in Fig. 2 inset. As shown in the inset, during initial 80 s since reaching the annealing temperature the maximum grows centered at $q = 0.62\ nm^{-1}$.

The presence of SAXS interference maximum is an evidence of non-random spatial arrangement of the scattering objects and the shift of the peak maximum accounts for increase of the objects' spacing. The average spacing L can be estimated from $L \approx 2\pi/q_m$, where q_m is the magnitude of the q-vector corresponding to the maximum of the SAXS signal. The observed SAXS spectra features are characteristic for systems undergoing phase separation by a spinodal mechanism. According to Cahn's linear theory of spinodal decomposition during early stages of phase separation a compositional fluctuations of constant wavelength increase spontaneously with time. This prediction is consistent with the results demonstrated in the inset of Fig. 2. The compositional fluctuation wavelength L evaluated from $L = 2\pi/0.62\ nm^{-1}$ is equal approximately 10 nm which is in agreement with the typical compositional wavelength values predicted by theory of spinodal decomposition [21].

During late stages of phase separation the coarsening of the decomposed regions occurs at their constant volume fraction. In the coarsening stage both decomposed region size D and spacing L increase at the same rate. Further both quantities change with time like t^a [22]. The value of exponent a is model-dependent and range from 1/6 for cluster coagulation [23] to 1/3 for Lifshitz and Slyozov coarsening mechanism [24]. The above feature of the phase separation is often called a "dynamical scaling". The

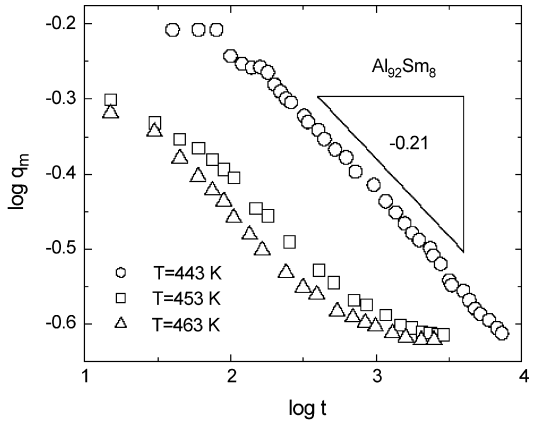

Fig. 3. $\log q_m$ vs. $\log t$ for $Al_{92}Sm_8$ annealed at three temperatures. The slope of plot for 443 K is indicated.

scaling hypothesis can be verified by plotting $\log q_m$ versus $\log t$ and $\log D$ versus $\log t$. Both plots are expected to be linear with the slope equal $|a|$. Fig. 3 presents the $\log q_m$ versus $\log t$ plots for three annealing temperatures. The plot for 443 K is linear over two time decades with the slope of -0.21. At higher temperatures the slope decreases rapidly and finally reaches zero.

The size of the scattering objects can be evaluated from the Guinier approximation [25] where $I(q) \propto \exp(R_g^2 q^2/3)$ with R_g standing for a radius of gyration. For the spherical objects of size D, $R_g = \sqrt{3/20}D$. Fig. 4 presents the $\log R_g$ versus $\log t$ plots for the same annealing temperatures as in Fig. 4. Like in Fig. 3 the plot for 443 K is linear with the slope equal 0.20 while for higher annealing temperatures the slope decreases down to zero.

Comparing Figs. 3 and 4 it can be concluded that the scaling hypothesis is confirmed in wide time range for 443 K with the time exponent of $a \approx 0.20$. At higher temperatures the coarsening process is rapidly blocked which is manifested by the decrease of exponent a. This feature will be discussed in further part of this paragraph.

Fig. 5 shows the time evolution of the WAXS spectra of the $Al_{92}Sm_8$ amorphous alloy during annealing

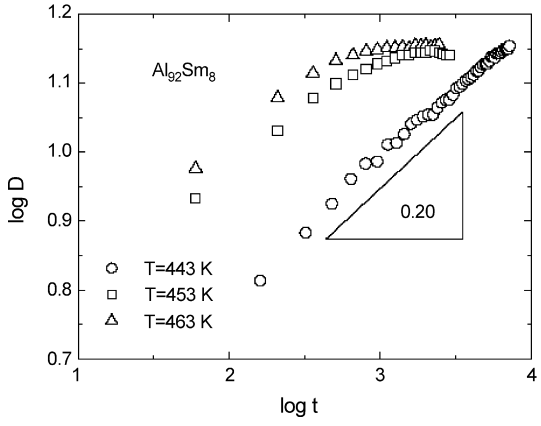

Fig. 4. $\log R_g$ vs. $\log t$ for $Al_{92}Sm_8$ annealed at three temperatures. The slope of plot for 443 K is indicated.

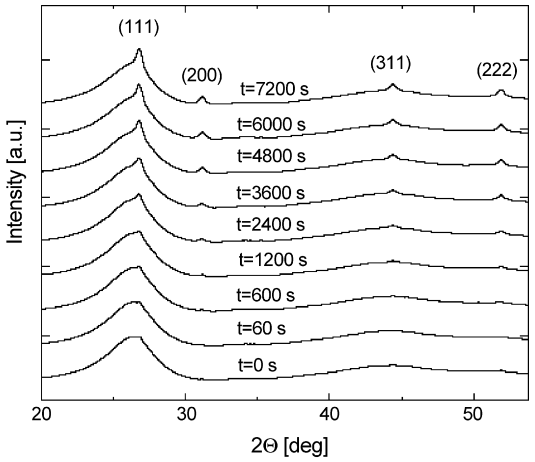

Fig. 5. Evolution of diffraction spectra of amorphous $Al_{92}Sm_8$ alloy during annealing at 443 K. The fcc-Al Bragg peaks are indexed.

at 443 K. The WAXS data give evidence of the amorphous → amorphous + fcc-Al transformation. From the diffraction data we calculate mean crystalline grain size from the standard Scherrer formula and the crystalline phase volume fraction using the recently proposed approach basing on the partial scattered intensities and X-ray properties of the constituent elements [9]. The average crystal size evolution for different temperatures are presented in Fig. 6 together with the size results evaluated from the SAXS data using the Guinier method assuming spherical shape of scattering objects. The inset in Fig. 6 shows the corresponding crystalline volume fraction calculations results. While the crystalline volume fraction increases progressively the mean grain size has a step-like character indicating a very fast growth in the initial stage of single grain evolution followed by a rapid growth arrest. Dark-field TEM image of $Al_{92}Sm_8$ sample annealed at 460 K for 1200 s is shown in Fig. 7. The mean nanocrystal size determined from the micrograph is 11.5 ± 1.5 nm which is fully consistent with the results of the Scherrer method. The above observations show that the nanocrystallization process is controlled by nucleation rate. A

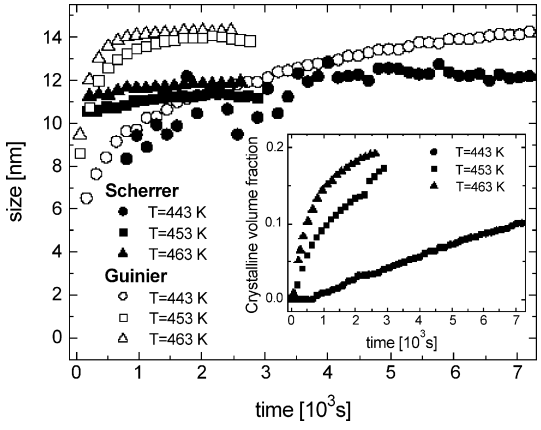

Fig. 6. The mean nanocrystal size using Scherrer method (full symbols) together with results of average size of scattering objects obtained from Guinier approximation. The inset shows the crystalline volume fraction evaluated using method proposed in Ref. [9].

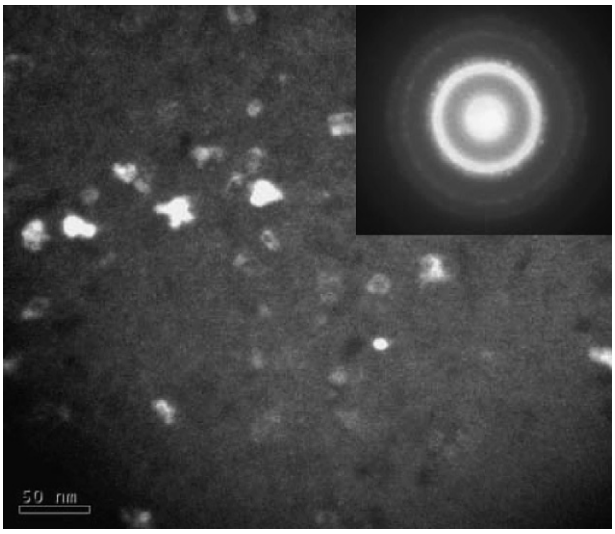

Fig. 7. Dark-field TEM image of $Al_{92}Sm_8$ sample annealed at 460 K for 1200 s. The mean nanocrystal size determined from the micrograph is 11.5 ± 1.5 nm. The inset shows the SAED pattern.

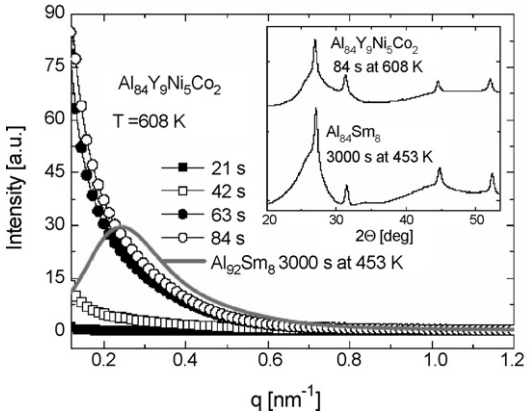

Fig. 8. SAXS spectra development of $Al_{84}Y_9Ni_5Co_2$ glass during annealing at 608 K. The spectrum of $Al_{92}Sm_8$ annealed for 3000 s at 453 K is also included. The inset shows the comparison of the diffraction spectra of the two heat-treated alloys.

detailed real-time X-ray diffraction study of nanocrystallization in Al–RE metallic glasses was presented in our previous papers [9,10].

The WAXS data show the progressive glass crystallization involving nanocrystal nucleation and thus the decrease of the average crystal spacing. On the other hand the SAXS results give an evidence of a continuous increase of the scattering objects' spacing characteristic for the coarsening stage of the phase separation. This apparent discrepancy can be resolved if amorphous phase separation and simultaneous crystallization of one of the decomposed phases is considered. Following this interpretation the SAXS signal is partially due to Al-rich decomposed regions and partially to nanocrystals nucleating preferentially inside the Al-rich regions. The probability of nucleation inside the Al-rich zone can be increased by faster atomic diffusion or/and by reduced interfacial energy for nucleation [20]. The nanocrystal size is constrained by the zones size because of the sluggish diffusion in the RE regions. The progressive crystallization slows down further glass decomposition by blocking the coarsening process. This effect is manifested by a decrease of the time exponent a for higher temperatures for which the crystalline volume fraction increases rapidly (see Figs. 3 and 4).

We suggest that the above mechanism is valid for $Al_{90}Y_{10}$, $Al_{92}Sm_8$, $Al_{91}Gd_9$, $Al_{91}Tb_9$ and $Al_{90}Sm_8Ni_2$ amorphous alloys, provided that all of them exhibit very similar SAXS/WAXS spectra evolution. A significantly different behavior was observed for $Al_{84}Y_9Ni_5Co_2$ glass where WAXS data indicate precipitation of fcc-Al while no interference maximum in small-angles regime was found (Fig. 8). Instead of that, the SAXS spectra of Al–Y–Ni–Co are typical for systems without spatial correlation of scattering objects. The random arrangement of precipitates is a characteristic feature of transformations initiated by nucleation and growth mechanism. The above results suggest that precipitation of the fcc-Al in Al–Y–Ni–Co glass does not involve amorphous phase separation but a nucleation and growth mechanism acts during devitrification. Interestingly, the TEM results for this alloy [26] prove that aluminium precipitates have nanometer size.

4. Conclusion

In conclusion we suggest that amorphous phase separation and crystallization of one of the decomposed phases is a possible mechanism of nanocrystallization in Al-based metallic glasses. The proposed model provides explanation of both ultra-high nucleation rate and rapid arrest of growth required for nanocrystalline microstructure formation. However, as demonstrated for the Al–Y–Ni–Co glass precipitation of fcc-Al phase can also be initiated by the nucleation and growth process.

Acknowledgments

Author is grateful to Prof. W. Botta for the TEM micrographs and for providing Al–Y–Ni–Co sample. Dr. J. Latuch is acknowledged for supplying part of the samples used in present study. The author would also like to thank Prof. A.R. Yavari for many stimulating discussions and to Dr. P. Panine of ESRF for professional help with SAXS/WAXS measurements and many valuable comments.

References

[1] A. Inoue, Prog. Mater. Sci. 43 (1998) 365.
[2] Y. He, S.J. Poon, G.J. Shiflet, Science 241 (1988) 1640.
[3] M. Calin, U. Köster, Mater. Sci. Forum 269–272 (1998) 749.
[4] G. Wilde, R.I. Wu, J.H. Perepezko, Proceedings of 22nd Risø International Symposium on Materials Science: Science of Metastable and Nanocrystalline Alloys Structure, Properties and Modelling, Risø National Laboratory, Roskilde, Denmark, 2001.
[5] K.F. Kelton, Philos. Mag. Lett. 77 (1998) 337.
[6] T.K. Croat, A.K. Gangopadhyay, K.F. Kelton, Philos. Mag. A 82 (2002) 2483.
[7] K.F. Kelton, T.K. Croat, A.K. Gangopadhyay, L.-Q. Xing, A.L. Greer, M. Weyland, X. Li, K. Rajan, J. Non-Cryst. Solids 317 (2003) 71.
[8] D.R. Allen, J.C. Foley, J.H. Perepezko, Acta Mater. 46 (1998) 431.
[9] J. Antonowicz, A.R. Yavari, G. Vaughan, Nanotechnology 15 (2004) 1038.
[10] J. Antonowicz, J. Non-Cryst. Solids 351 (30–32) (2005) 2383–2387.

[11] X.Y. Jiang, Z.C. Zhong, A.L. Greer, Mater. Sci. Eng. A 226–228 (1997) 789.
[12] C.-P.P. Chou, D. Turnbull, J. Non-Cryst. Solids 17 (1975) 169.
[13] S. Schneider, P. Thiyagarajan, W.L. Johnson, Appl. Phys. Lett. 68 (1996) 493.
[14] A.R. Yavari, Acta Metall. 36 (1988) 1863.
[15] H.S. Chen, Mater. Sci. Eng. 23 (1976) 151.
[16] L. Tanner, R. Ray, Scripta Metall. 14 (1980) 657.
[17] J. Piller, P. Haasen, Acta Metall. 30 (1982).
[18] R. Bush, S. Schneider, A. Peker, W.L. Johnson, Appl. Phys. Lett. 63 (1995) 1544.
[19] J. Löffler, W.L. Johnson, Appl. Phys. Lett. 76 (2000) 3394.
[20] U. Köster, Mater. Sci. Forum 235–238 (1997) 377.
[21] E.L. Huston, J.W. Cahn, J.E. Hilliard, Acta Metall. 14 (1966) 1053.
[22] K. Binder, P. Fratzl, in: G. Kostorz (Ed.), Spinodal Decomposition in Phase Transformations in Materials, Wiley-VCH, Weinheim, 2001, pp. 409–480.
[23] K. Binder, D. Stauffer, Phys. Rev. Lett. 33 (1974) 1006.
[24] I.M. Lifshitz, V.V. Slyozov, J. Phys. Chem. Solids 19 (1961) 35.
[25] A. Guinier, G. Fournet, Small-angle Scattering of X-rays, John Wiley and Sons, New York, 1995.
[26] N. Bassim, C.S. Kiminami, M.J. Kaufman, M.F. Oliveira, M.N.R.V. Perdigao, W.J.B. Filho, Mater. Sci. Eng. A 304–306 (2001) 332.